ASSESSMENT OF EARLY-STAGE GLAUCOMA WITH OPTICAL ATTENUATION COEFFICIENTS

By

Shuang Chang

Thesis

Submitted to the Faculty of the

Graduate School of Vanderbilt University in

partial fulfillment of the requirements

for the degree of

MASTER OF SCIENCE

in

Biomedical Engineering

December 16, 2023

Nashville, Tennessee

Approved:

Audrey Bowden, Ph.D.

Andrea Locke, Ph.D.

ACKNOWLEDGMENTS

TABLE OF CONTENTS

LIST OF TABLES

LIST OF FIGURES

CHAPTER 1

Introduction

1.1 Motivation and Objective

Glaucoma is characterized by the degeneration of the retinal nerve fiber layer (RNFL),[1] which can be assessed by thickness measurement on optical coherence tomography (OCT) B-scans.[2–4] However, detecting early-stage glaucoma remains a challenge. Due to biological variations in the eyes of healthy individuals, there exists an inherent overlap between the thickness of early-stage glaucomatous RNFL and healthy RNFL.[5, 6] More importantly, glaucoma-suspect patients represent a large portion of glaucoma patients seen at the clinics; however, current diagnostic tools lack the sensitivity in detecting early-stage changes in the suspect population. Therefore, there is a need for a new diagnostic biomarker to provide better indication of disease development in this population. In this thesis study, we aim to investigate the effectiveness of the optical attenuation coefficient (AC) and AC-derived parameters for detecting early-stage changes glaucomatous eye.

1.2 Summary of Chapters

Chapter 1 introduces the problem of glaucoma and the motivation behind the presented research, which is to enable detection of early-stage glaucoma.

Chapter 2 covers the clinical background and technical background for the topics discussed in this thesis work. Pathological changes in the retina during development of glaucoma, the current diagnostic tools available in the clinic, and the limitations of standard-of-care tools and emerging technologies in glaucoma detection are explained. The need for a quantitative biomarker is introduced. Next, the technical background of the proposed solution – attenuation coefficient (AC) – is discussed in detail, covering the definition of the AC, methods of AC estimation, and previous clinical demonstrations of AC for glaucoma assessment.

Chapter 3 presents a comparison study for two methods of AC extraction from clinical optical coherence tomography (OCT) B-scans collected from four study groups. The groups include healthy individuals, glaucoma-suspect patients, mild and severe stage glaucoma patients. The results show comparable performances of the two methods and reveal a decreasing trend in the calculated AC as disease stage progress.

Chapter 4 introduces novel depth-dependent AC parameters calculated from pixel-wise AC measurements. The new parameters are shown to further differentiate the early-stage population from the healthy group. Biological reasonings for the observed trends are discussed, which may relate to the changes in axon density and capillary density as a function of depth and disease severity.

Chapter 5 summarizes major findings of this thesis research and suggests future directions for further validation and eventually clinical translation. The impacts of the thesis research are also presented.

This thesis document is adapted from my two first-author publications:

Shuang Chang, Audrey K. Bowden, "Review of methods and applications of attenuation coefficient measurements with optical coherence tomography," J. Biomed. Opt. 24(9), 090901 (2019)

Shuang Chang, Clara Murff, Theodore Leng, Sylvia L. Groth, and Audrey K. Bowden, "Depth-resolved extraction of optical attenuation for glaucoma assessment in clinical settings: a pilot study," Biomed. Opt. Express 13, 4326-4337 (2022)

CHAPTER 2

Background and Related Work

2.1 Glaucoma

2.1.1 Pathological Changes in the Retina

Glaucoma, a type of optic neuropathy, is a leading cause of irreversible vision loss in the world and affects more than 70 million people worldwide.(1) Glaucoma is caused by the degeneration of retinal ganglion cells. The ganglion cells are neurons of the central nervous system whose cell bodies reside in the inner retina and whose axons form the optic nerve. An elevation of intraocular pressure (IOP) is normally seen in glaucoma patients, which is responsible for the death of retinal ganglion cells, as illustrated in Figure 1. In healthy eyes, there is a balance between aqueous humor secretion through ciliary body and its drainage through trabecular meshwork and uveoscleral outflow pathways. In cases of primary open angle glaucoma (POAG), which accounts for more than 80% of glaucoma cases, resistance to the outflow of aqueous humor increases at the trabecular meshwork, which leads to elevation of intraocular pressure in the anterior chamber. The pressure-induced stress and strain compress and deform lamina cribrosa structure in the optic nerve and thus interrupt the trophic delivery to retinal ganglion cells, leading to cell death and degeneration of the optic nerve.(7) Because POAG is slow progressing, symptoms and damage often are left unnoticed until late stages.

(A) Build-up of aqueous humor.　　(B) Degeneration of optic nerve.
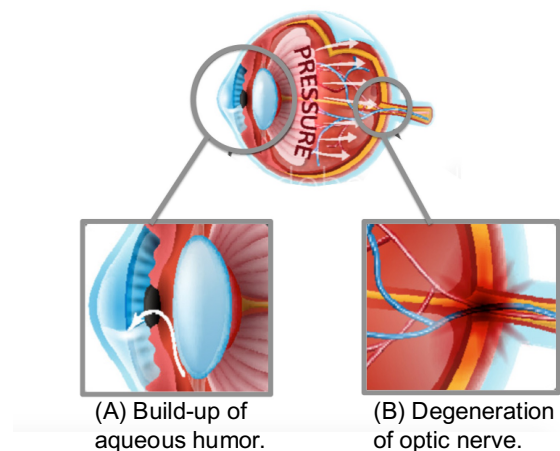
Figure 1. Glaucomatous eye is caused by the blockage of aqueous humor drainage canal (A) and thus leads of intraocular pressure elevation, which results in damage of the optic nerve (B).

Glaucoma can occur in all age groups; however, it is more commonly seen in the elderly (age 80+), with a varying level of severity from a mild form of vision loss to complete vision loss. Typical glaucomatous vision is illustrated in Figure 2. Traditionally, the gold standard of glaucoma detection is the intraocular pressure test using a tonometer. Glaucomatous eyes normally have an IOP above 22 mmHg, while healthy eyes have a pressure range between 12 and 22 mmHg. However, it has been found that 25% to 50% of glaucoma patient have an IOP less than 22 mmHg. Therefore, a large number of glaucoma patients remain undiagnosed until late stages, where rapid deterioration of ganglion cells occurs and leads to irreversible vision loss.(8)

Figure 2. Normal vision vs. glaucomatous vision. Patients with glaucoma suffer from varying degrees of peripheral vision loss based upon severity of disease.

2.1.2 Detection of Early-Stage Glaucoma

Due to the progressive nature of glaucoma, early detection of the disease is critical to preserve vision. A comprehensive eye examination is often required for patients who are potentially affected by glaucoma. Classical examinations such as the visual field test are largely subjective and suffer from variability.(9) Therefore, many researchers have worked on developing more objective diagnostic tools for measuring the changes in microstructures of the eye, such as the optic nerve head and retinal nerve fiber layer (RNFL). Extensive studies have been conducted on imaging tools, including confocal scanning laser ophthalmoscopy,(10) scanning laser polarimetry(11) and optical coherence tomography (OCT).(12)

2.2 OCT as a Promising Technology in Glaucoma Detection

OCT is an established technique that provides non-invasive, volumetric and real-time *in vivo* images of tissue microstructure.(13) The general strategy for OCT is based on low-coherence interferometry. Light incident on the tissue of interest is collected in a backscattering geometry and combined with light returning from a reference path. The resulting signal is presented in the form of an A-scan, which describes the relative position in depth and intensity of reflecting structures in the tissue. OCT provides a profile of the underlying tissue microstructure, generating an optical biopsy (B-scan), allowing non-invasive imaging of the tissues with high resolution and diagnostic accuracy. As a result, OCT has been shown as a promising technique to provide structural changes in the eye, specifically in imaging the anterior segment and the retinal layers.

Traditional OCT has long been used to visualize morphological changes in the retina.(14) An elevation of intraocular pressure is normally seen in glaucoma patients, leading to the death of retinal ganglion cells. (15) This degenerative process can be detected clinically by measuring the thickness of the RNFL with OCT, making it a critical technology for glaucoma diagnosis.

Although measurement of RNFL thickness effectively differentiates glaucomatous eyes from healthy eyes,(2–4) a large variation exists among the thickness measurements in healthy individuals due to structural differences such as myopia(16–18) and optic disc size.(5, 6) This inherent overlap between the RNFL thicknesses of some healthy eyes and early-stage glaucomatous eyes leads to challenges in early glaucoma detection. As a result, researchers have sought to investigate whether other parameters, such as ganglion cell layer thickness, RNFL reflectance, and volumetric analysis of the retina, may be more reliable indicators of early-stage glaucoma.(18–20)

2.3 Optical Attenuation Coefficient Serves as a Diagnostic Biomarker in Glaucoma

In addition to the thinning of the RNFL that can be visualized on OCT B-scans, the death of retinal ganglion cell axons in glaucoma leads to changes in the scattering property of the RNFL.(21)(22) This change is hypothesized to be caused by the reduction in axon density in diseased RNFL,(10, 15, 23) and it can be

quantified through measurement of the optical attenuation coefficient (AC). The AC measures how quickly incident light is attenuated when passing through a medium and is a function of the underlying medium properties. AC values can serve as an indicator for microscopic changes within tissues.(24–30)

2.3.1 Definition of Attenuation Coefficient

The AC measures how quickly incident light is attenuated when passing through a medium and is a function of the underlying medium properties. Loss of light in tissue can be caused by absorption, scattering or a combination of both. When propagating through a medium, the irradiance of the light beam follows the equation:

$$I = I_0 e^{-\mu z}, \qquad (1)$$

where z is the distance light travels into tissue and μ is the AC of light in that tissue. When μ is small, the irradiance of light will experience a slow exponential decay, as happens when the tissue sample has low absorption and weakly scattering properties. In contrast when μ is large, the irradiance will decrease quickly and exponentially, as happens in highly scattering or absorbing tissue types. Because the AC is an underlying tissue property, accurate estimation of the AC allows differentiation of dissimilar tissue types. This information is complementary to information about the tissue microstructure provided by standard OCT B-scans, which represents the backscatter intensity at each depth. In fact, a true picture of the backscatter intensity at each depth should take into account the fact that the light incident at each depth of the tissue is reduced by the attenuation of light from anterior structures. Figure 3 shows a conventional OCT B-scan of a healthy human retina compared to its AC mapping. Note that to some degree, the intensity of scattering correlates with the magnitude of the attenuation coefficient, as one would expect.
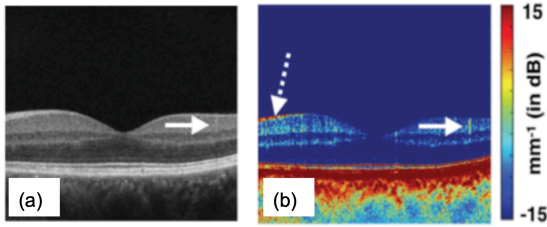
Figure 3. Images of human retina obtained by commercialized OCT (a) in comparison with AC mapping (b). Dashed arrow in (b) points to the retinal nerve fiber layer of the retina. Solid arrow in (a) and (b) points to a shadow resulting from a superficial retinal blood vessel (Adapted from reference (31)).

2.3.2 Methods of Derivation

Multiple methods have been proposed to extract AC measurements from OCT images. These methods are associated with two general models that have been proposed: the single-scattering (SS) model (32, 33) and the multiple-scattering (MS) model (34); the tissue type of interest determines which model should be used. The SS model assumes the backscattering of photons only occurs once and is applicable to AC measurement in weakly scattering tissue samples or superficial layers of a highly scattering tissue sample, such as human axillary lymph nodes (35) and the retinal nerve fiber layer (36). The MS model takes multiple backscattering events and larger probing depths (37) into consideration, and it has been used for extracting optical properties from human skin (38) and blood vessels (39). The SS model is more widely used, especially as single scattering is a general assumption of OCT image reconstruction.

Within the SS model, two main approaches for AC estimation have been described, which are known as curve-fitting (CF) and depth-resolved (DR) (32, 33), respectively. The general idea behind CF methods is to fit the exponential decay described by Eq. 1 to the A-scan data of interest and determine the AC as the exponential parameter that best fits this curve. In contrast, DR methods use differences in the intensity of adjacent voxels to recover the amount of attenuation that occurs on a per-pixel basis. Both approaches have been successfully applied to many clinical applications.

2.3.2.1 Curve-Fitting Method

The CF method was first introduced by Faber et al (33). The detected OCT signal is purported to follow the Lambert-Beer Law shown in equation (1). In order to accurately extract AC values, Faber et al. also take the effect of the confocal point spread function into consideration by introducing the following expression:

$$h(z) = \left(\left(\frac{z - z_{cf}}{z_R} \right)^2 + 1 \right)^{-1} , \qquad (2)$$

where h is the confocal function, z_{cf} denotes the focal plane depth and z_R is the apparent Rayleigh range. The term z_R is defined as $z_R = \alpha n z_r$, where $\alpha = 2$ for diffuse reflection ($\alpha = 1$ for specular reflection), n is the index of refraction of the tissue sample, and z_r is the Rayleigh range of the scanning lens. Faber showed that when the focal plane of the optical system is located within the sample, the confocal function needs to be taken into account in order to best describe the resulting OCT signal. Therefore, by combining equations (1) and (2), Faber concludes that the recorded OCT signal intensity can be modeled as:

$$I(z) \propto h(z) e^{-2\mu z} , \qquad (3)$$

where the factor of 2 accounts for the light being attenuated twice due to the round-trip backscattering event measured with OCT. The estimated AC (μ) in a given medium can then be found by fitting the averaged OCT A-scans to the model described in equation (3). The CF algorithm used in Faber's method finds the maximum likelihood estimation by minimizing χ^2, which is given by:

$$\chi^2 = \sum_{i=1}^{N} \left(\frac{y_i - f\left(x_i ; a_1 ... a_M \right)}{\sigma_i} \right)^2 , \qquad (4)$$

Where y_i are the recorded intensities, x_i are depths, f is the model written in equation (2), and a_j are the fitted parameters to be determined (in this case the fitted parameters are μ and a multiplier A to equation (2)). An example of an application of the CF method is shown in Figure 4, where different types of atherosclerotic tissue can be differentiated (27) on the basis of different attenuations.
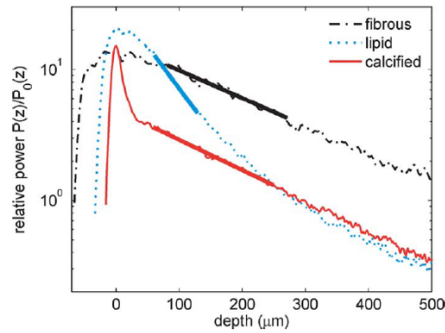
Figure 4. CF method applied to ex vivo atherosclerotic plaque characterization, where thick lines show the fitting over areas of interest (Adapted from reference (27)).

In 2012, Vermeer et al. applied and updated Faber's CF method for extraction of the AC in the retinal nerve fiber layer (RNFL) of the eye by using the retinal pigment epithelium (RPE) as a reference layer to normalize the OCT data (40). The reason for normalization is that before reaching the retina, the incident light is first attenuated by the anterior segment and the vitreous region of the eye, so the power of light that reaches the top layer of the retina (RNFL) is already a fraction of the initial incident light power. In essence, they recognized that the total power incident on the retina fluctuates due to the differences in opacity and the amount of vitreous humor the light must travel through (i.e., for different positions on the retina). Because the RPE is a highly scattering layer in the retina that is assumed to be uniformly scattering, it was

5

chosen as a reference to normalize the total OCT signal of the RNFL.

The referenced CF method can be understood in the following way. According to Lambert-Beer's law, the differential equation for an attenuated light beam is given by (40):

$$dI(z) = -\mu(z)I(z)dz \quad (5)$$

which makes μ a depth-dependent AC and establishes a linear relationship between the incident light intensity and the attenuated light intensity. The power of incident light at depth z into the medium can be expressed as: $I(z) = I_0 e^{-\mu z}$, where μ is the attenuation coefficient specific to the medium. The backscattered light is a fraction of the attenuated light, which has a power of $\alpha\mu I_0 e^{-\mu z}$ at depth z, and a power of $\alpha\mu I_0 e^{-2\mu z}$ at the detector. The additional factor of 2 accounts for the roundtrip attenuation.

By integrating over a depth range d, the total power of backscattered light from this depth range can be expressed as:

$$S = \int_{z=0}^{d} \gamma\alpha\mu I_0 e^{-2\mu z} \, dz = \frac{\gamma\alpha I_0}{2}\left(1 - e^{-2\mu d}\right) \quad ,(6)$$

where S is the total OCT signal, I_0 is the incident light intensity, γ is the conversion factor that converts the detected backscattered OCT signal to digital signal, and α is the fraction of light arriving at the layer of interest. Therefore, the total OCT signal backscattered from the RNFL is given by:

$$S_{RNFL} = \frac{\gamma\alpha_{RNFL} I_0}{2}\left(1 - e^{-2\mu_{RNFL} d_{RNFL}}\right)$$

, and the total OCT signal reflecting from the RPE layer is:

$$S_{RPE} = \frac{\gamma\alpha_{RPE} I_0}{2}\left(1 - e^{-2\mu_{RPE} d_{RPE}}\right)e^{-2\mu_{RNFL} d_{RNFL}}$$

, assuming the intensity loss between the RNFL and RPE layers is negligible. Then Vermeer et al. computes the ratio R of the total signal in the RNFL over the total signal in the RPE:

$$R = \frac{S_{RNFL}}{S_{RPE}} = \frac{\dfrac{\gamma\alpha_{RNFL} I_0}{2}\left(1 - e^{-2\mu_{RNFL} d_{RNFL}}\right)}{\dfrac{\gamma\alpha_{RPE} I_0}{2}\left(1 - e^{-2\mu_{RPE} d_{RPE}}\right)e^{-2\mu_{RNFL} d_{RNFL}}} = \frac{\alpha_{RNFL}\left(e^{2\mu_{RNFL} d_{RNFL}} - 1\right)}{\alpha_{RPE}\left(1 - e^{-2\mu_{RPE} d_{RPE}}\right)} . \quad (7)$$

Because the author assumes that the attenuation in the RPE and the thickness of the RPE, d_{RPE}, are constant for a given person, the above expression can be simplified to

$$R = \beta\left(e^{2\mu_{RNFL} d_{RNFL}} - 1\right), \quad (8)$$

where β is a constant and equals $\dfrac{\alpha_{RNFL}}{\alpha_{RPE}\left(1 - e^{-2\mu_{RPE} d_{RPE}}\right)}$. Then β and μ_{RNFL} can be estimated by fitting the model to the ratio R determined from intensity measurements, and the optimal fit is found by minimizing the error defined by the L^1-norm of the difference between the model and the actual data:

$$\{\beta, \mu\} = \underset{\beta, \mu}{\arg\min} \sum_i \left| \log\left(\frac{\beta\left(e^{2\mu d_i} - 1\right)}{R_i}\right) \right| . \quad (9)$$

6

With known β, the attenuation of the RNFL layer can be solved as:

$$\mu_{RNFL} = \frac{\log\left(\frac{R}{\beta}+1\right)}{2d_{RNFL}} . \qquad (10)$$

This work underscores the importance of understanding the physiology of the underlying tissue to extract meaningful measurements of the AC.

2.3.2.1 Depth-Resolved Method

One drawback of the CF method is that a large amount of data is needed to accurately fit a curve, leading to an inability to extract values over small tissue regions. In the past few years, however, new approaches have emerged for extracting AC that offer higher resolution than CF. For example, the DR model developed by Vermeer et al. (32) in 2014 allows for estimation of the AC for each pixel, which enables pixel-wise tissue-type differentiation in both homogeneous and heterogeneous tissues. This is in contrast to the CF method, which only works with a single, uniform tissue type or requires an additional step of segmenting the tissue manually or using automated methods (32, 33).

The DR method relies on two fundamental assumptions: first, light is attenuated almost completely within the measured imaging depth range; second, the fraction of backscattered light collected by the photo-detector of the OCT system from the attenuated light is a constant (32). Note that the latter assumption may not be true in the case of significant attenuation due to absorption. Vermeer's method enables pixel-wise estimation of the OCT data, and this is also based on the SS model. According to the linear relationship between the incident light intensity and the attenuated light intensity in equation 5, at the zero-depth condition (z =0, boundary condition), equation (5) can be solved as:

$$L(z) = I_0 e^{-\int_0^z \mu(u)du} , \qquad (11)$$

where $L(z)$ is the attenuated light intensity at depth z and the incident light intensity is given by I_0. The actual detected OCT signal can be expressed in equation (12),

$$I(z) = A\kappa\mu(z)I_0 e^{-2\int_0^z \mu(u)du}, \qquad (12)$$

where the factor 2 accounts for the round-trip attenuation of light in tissue, A is the constant ratio of backscattered light to total attenuated light, and κ is the conversion factor during digitizing and integrating of the signal. Then the AC in a given region of the medium can be estimated by solving for $\mu(z)$ with a depth range D:

$$\mu(z) \approx \frac{I(z)}{2\int_z^D I(u)du} . \qquad (13)$$

Equation (13) allows definition of the AC on a continuous domain, so if a pixel-wise coefficient value is desired, then the intensity measurements need to be integrated and average over the pixel size Δ, which is commonly related to the coherence length of the light source. When the integral is solved for each pixel,

the expression can be written as: $\mu[i] = \frac{1}{2\Delta}\log\left(1+\frac{I[i]}{\sum_{i+1}^{\infty} I[i]}\right)$. Simplifying the $\log(1+x)$ term with a first-order linearization, which is equivalent to x assuming x is small, the expression can be re-written as:

$$\mu[i] \approx \frac{I[i]}{2\Delta\sum_{i+1}^{\infty}I[i]}. \qquad (14)$$

Vermeer's DR method improves estimation of the AC in that it does not require fitting a curve to OCT signals, which may be affected by noise in the data. Pixel-wise estimation enables application on multi-layered tissues, as shown in Figure 5, and because this method compares the local OCT signal to the integral of signals from deeper layers, it allows accurate estimation from thin or superficial layers.
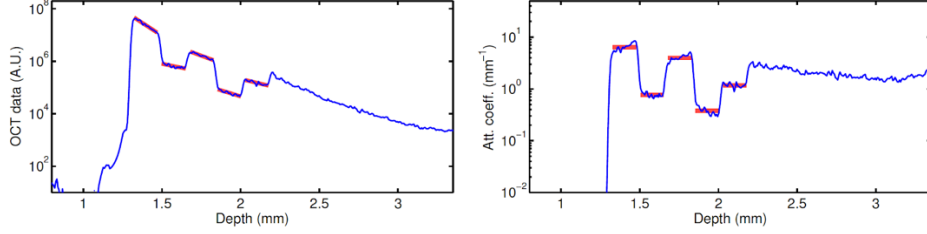
Figure 5. Depth profile (A-scan) of a layered phantom (a) and the pixel-wise attenuation estimated using the DR method (b).With DR estimation, pixel-specific AC measurement can be achieved. Thick red lines indicate depth ranges where measurements were taken (Adapted from (32)).

Sensitivity fall-off is a phenomenon that affects the perceived OCT intensity in SD-OCT systems. This phenomenon leads to a decrease of system sensitivity with depth due to the greater reduction of fringe visibility by the finite resolution of the spectrometer at higher fringe frequencies (41). The effect caused by this sensitivity decay was also considered in Vermeer's method, where they employ a Gaussian model of imaging depth z and width σ :

$$S(z) = e^{\frac{-z^2}{\sigma^2}}, \qquad (15)$$

where the width of the Gaussian model σ can be determined from sensitivity measurements. Vermeer's group corrects this fall-off effect by dividing each A-line measurement by this sensitivity factor *S(z)*.

One limitation of the classical depth-resolved method is that it does not take the confocal function into consideration. In low AC regions, the dependency on the confocal function is significant. Vermeer et al. circumvent the need to account for confocal parameters in their algorithm by placing the focal plane above the sample (i.e., with the effect of forcing the region of interest to be acquired in a domain where the confocal function is almost constant), but this leads to over-estimation in low-attenuation regions.

In 2016, Smith et al. introduced a modification of the depth-resolved method, termed the Depth-resolved Confocal (DRC) method, that accounts for both the confocal function $h(z)$ and sensitivity fall-off effect in processing the OCT signal (42). The DRC method addresses the issue with the depth-resolved method that accurate ACs can only be extracted when the focal plane is not located in the tissue sample, a condition that does not hold true for many common clinical applications and also leads to reduced signal to noise ratio (SNR) (32). With DRC, AC can be extracted while the focal plane is placed within the sample.

In Smith's work, a more comprehensive sensitivity fall-off model(41) is used, allowing more accurate estimation of AC to be extracted than the Gaussian model used by Vermeer's Depth-resolved method. The comprehensive model accounting for the sensitivity fall-off effect used in Smith's paper is expressed as *S(z)*:

$$S(z) = \left(\frac{\sin\zeta}{\zeta}\right)^2 \cdot \exp\left(-\frac{\left(\frac{\delta\lambda}{\Delta\lambda}\right)^2}{2\ln 2}\zeta^2\right). \qquad (16)$$

8

In this model, $S(z)$ is the magnitude of signal decay and $\zeta = \dfrac{\pi \cdot z}{2 \cdot z_{RD}}$ describes the depth z, normalized by the maximum ranging depth z_{RD}, which is equal to $\dfrac{\lambda_0^2}{4\Delta\lambda}$, where λ_0 is the central wavelength of the light source, $\Delta\lambda$ is the wavelength spacing between pixels, and $\delta\lambda$ is spectral resolution of spectrometer (FWHM). By combining equations (2), (12) and (16), the final light attenuation model used in Smith's work becomes:

$$I_{fh}(z) = S(z)h(z)\kappa L_0 \alpha \mu(z) e^{-2\int_0^z \mu(\theta)d\theta} , \quad (17)$$

where the confocal function $h(z)$ is determined experimentally with known locations of the focal plane and the Rayleigh range of OCT system, and the parameters of the sensitivity fall-off function were determined by imaging a neutral density filter and fitting the data to Equation 15. With the updates Smith et al. made in DRC, AC measurement can be extracted without restrictions on focal plane position, which permits imaging with enhanced SNR and enables AC measurement for a wider range of clinical applications.

2.3.3 Previous Demonstrations

Vermeer *et al*. and van der Schoot *et al*. applied measurement of the AC to differentiate glaucomatous tissue from normal retinal tissue, specifically in the retinal nerve fiber layer (RNFL) (22, 36). Vermeer et al. used CF, with the RPE serving as a reference layer (22), to extract the AC values for healthy, mildly glaucomatous, moderately glaucomatous and severely glaucomatous eyes (AC values of 4.78 ± 0.46 mm^{-1}, 4.09 ± 0.34 mm^{-1}, 3.14 ± 0.22 mm^{-1} and 2.93 ± 0.33 mm^{-1}, respectively). The AC results show that the AC in the RNFL decreases as the level of glaucoma progresses. van der Schoot et al. hypothesize that the decrease in AC is related to pathological changes in the eye and is due to the reduction of nerve fiber density in glaucomatous RNFL that occurs when ganglion cells degenerate (36), (43). In previous studies, the decreased density has been associated with RNFL tissue properties changes such as the reduction of birefringence and reflectance in the RNFL even prior to the thinning (10, 19, 44). The hypothesis is that the decrease in ganglion cell axon density also leads to less scattering in the RNFL, which in turn causes diminished AC values. As glaucoma stage advances, the axon density will continue to decrease, resulting in reduction of the AC. Therefore, the AC can serve as an indicator of glaucoma presence and severity even prior to when structural changes can be visualized. Vermeer et al. also generated *en face* AC maps, which allow visualization of attenuation patterns in the retina of both healthy and glaucomatous eyes along with corresponding thickness maps, as shown in Figure 6 (22). Vermeer concluded that AC measurement provides comparable results to the thickness measurements and shows promising potential in early glaucoma assessment and diagnosis.
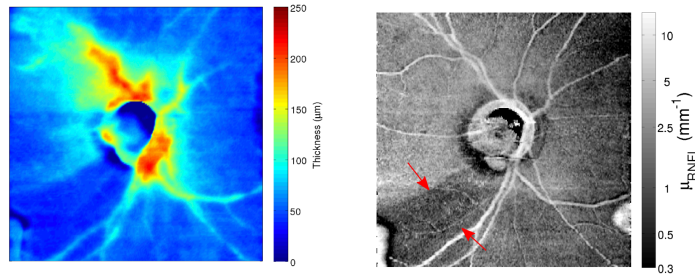
Figure 6. RNFL thickness mapping (left) vs. RNFL AC plot (right) of a glaucomatous eye. Red arrow indicates the location of affected tissue, which coinciding with reduced thickness in infero-temporal region (Adapted from (40)).

While these previous studies have shown a significant difference between AC_{RNFL} values in healthy and glaucomatous eyes ($p < 0.001$),(22, 23) the method used in those relies on determining the intensity ratio between two scattering layers – the RNFL and the retinal pigment epithelium (RPE). For convenience, that algorithm will be referred to as the layer intensity ratio (LIR) method – a curve-fitting-based method. Unfortunately, LIR requires segmentation of the retina, an extra step in the processing pipeline that typically requires manual input.

New variations of a depth-resolved method of extracting the AC have been introduced recently, including the AutoConfocal method.(32, 42, 45) These methods remove the need for segmentation and increase the resolution of the AC measurement by allowing pixel-wise estimation,(32) which can be important in detecting smaller changes that occur in early glaucoma.

In the following chapters, we explore the potential of the AutoConfocal + DRC method, henceforth referred to as the DRC method, to differentiate glaucomatous disease states in volunteers with normal vision, glaucoma suspects, and patients with mild and moderate/severe glaucoma. Our primary goal is to demonstrate the degree to which DRC can differentiate healthy from glaucomatous individuals compared to LIR algorithm. In addition, our inclusion of glaucoma-suspect patients allows us to investigate the clinical value of the AC of the RNFL for early glaucoma detection, which has not been previously explored. Lastly, with the depth-resolved information we extracted from the DRC analysis, we introduce new depth-dependent parameters that show promise as potential diagnostic biomarkers.

CHAPTER 3

Comparison of Curve-Fitting and Depth-Resolved Methods in Deriving AC of the RNFL

3.1 Abstract

Optical coherence tomography (OCT) is a standard-of-care tool to image the retina for detection and monitoring of the development of glaucoma. Thickness measurements from OCT intensity images have several drawbacks and were shown to be insufficient to detect early-stage glaucoma. The optical attenuation coefficient (AC) is a tissue-specific parameter that could serve as diagnostic biomarker for glaucoma. Several extraction methods of AC have been proposed. In this chapter, we explore how two popular AC extraction methods – curve-fitting and depth-resolved based methods – compare in measurement of the AC of the RNFL. We also report measurements of the AC in glaucoma patients, glaucoma suspects as well as healthy individuals.

3.2 Materials and Methods

3.2.1 Human Subject Recruitment

With approval from the Institutional Review Board of Vanderbilt University (IRB #190937), we recruited patients presenting to the Vanderbilt Eye Institute who were previously diagnosed with glaucoma or high risk of glaucoma based on standard-of-care methods, including a visual field test, biomicroscopy and OCT. Informed consent was obtained after thorough explanation of the study. Glaucoma severity was determined by the mean deviation (MD) of the visual field test (Humphrey field analyzer II, Carl Zeiss Meditec), where mild glaucoma cases had an MD ranging from 0 to -6.0 dB and moderate/severe cases had an MD worse than -6.0 dB. Eyes with visual acuity (VA) worse than 20/50 were excluded from analysis. Glaucoma suspects were identified by clinicians: these patients had high risk of glaucoma by showing some suspicious feature during exam, such as optic nerve asymmetry, a family history of glaucoma, or a high intraocular pressure (IOP), but had not shown functional damage on the visual field test or thinning of the RNFL on OCT scans. Age-similar healthy volunteers were recruited as a control population. For inclusion, healthy participants needed to have a healthy eye history (except for uncomplicated cataract surgery), IOP of 21 mm Hg or lower, no signs of glaucoma when examining the optic nerve appearance and 20/25 or better VA. Individuals with a visually significant cataract (without receiving surgery) were excluded from the study, to avoid poor signal quality.

3.2.2 Participant Imaging

For each eye, we collected three B-scans in succession in a single sitting, with each of the three scans varying the depth of the focal plane to allow extraction of the confocal parameters from the AutoConfocal algorithm.(31) All scans were acquired on the Zeiss Cirrus 5000 Spectral Domain OCT machine (Carl Zeiss Meditec, Inc, Dublin, CA). A built-in eye-tracker was used during image acquisition to ensure that the scans were collected from the same location in the eye. The Cirrus scan was taken as one line of a 9-mm scan tilted at 7 degrees, centered on the optic nerve and the fovea.

3.2.3 Manual Segmentation

To demonstrate the comparative performance of DRC vs LIR for differentiating healthy from glaucomatous individuals, we performed manual segmentation of the inner and outer surface of the RNFL and of RPE of each B-scan, as required by the LIR algorithm. One annotator, while masked to clinical data, manually labeled the RNFL and RPE on a photo-editor software (Digital Ruby, LLC. *YouDoodle Pro*. Version 7.9.0) and then imported the labeled B-scans to a custom MATLAB (The Math Works, Inc. *MATLAB*. Version 2018b) algorithm for extraction of the layer information. The annotation was validated by another observer, who was also masked to the clinical information. Note that the outer RPE surface (purple line in Figure 7, left column) was segmented by hand while the inner RPE surface (blue line) was marked by offsetting the outer surface by a fixed number of pixels, as has been done in prior work.(23) This method assumes that the RPE has a constant thickness in the B-scan. The extracted surfaces were smoothed with local regression

using a second-degree polynomial model and a weighted linear least squares algorithm to remove non-biologically realistic features in the manual segmentation (e.g., sharp edges and straight-line segments).
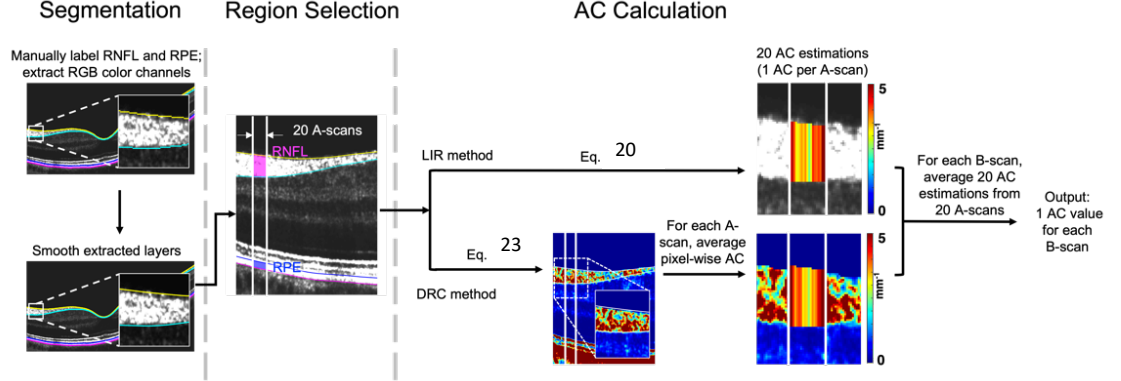

Figure 7. Flowchart of data processing steps to acquire AC estimations from B-scans

3.2.4 Region Selection

The target site of analysis was a 20-A-scan region located at a 1.3-mm distance from the center of the optic nerve head (ONH),(23) shown in the middle column of Figure 7. This region was selected because it is the most clinically relevant region on the retina for RNFL assessment: most RNFL thickness measurements are performed on a ring-shaped region 1.3 mm or 1.7 mm away from the ONH.(11, 46)

3.2.5 AC Calculation

The steps we took to obtain the AC estimations with the LIR method and the DRC method are illustrated in the right column of Figure 7.

AC calculations with the LIR method: This method is a derivation based on the original curve-fitting AC algorithm introduced by Faber et al.: the light intensity is modeled as

$$I(z) \propto h(z)e^{-2\mu z}, \quad (18)$$

where h is the confocal function, $h(z) = \left(\left(\frac{z - z_{cf}}{z_R} \right)^2 + 1 \right)^{-1}$, and z_{cf} and z_R denotes the system parameters,

the focal plane depth and the apparent Rayleigh range, respectively. In the papers by Vermeer(22, 40) and van der Schoot(47) in 2012, they extended the original curve-fitting method to extract the AC from the RNFL, utilizing the RPE as the reference layer, where intensity ratios of the RNFL and RPE can be expressed as:

$$R = \frac{S_{RNFL}}{S_{RPE}} = \frac{\frac{\gamma \alpha_{RNFL} I_0}{2}(1 - e^{-2\mu_{RNFL} d_{RNFL}})}{\frac{\gamma \alpha_{RPE} I_0}{2}(1 - e^{-2\mu_{RPE} d_{RPE}}) e^{-2\mu_{RNFL} d_{RNFL}}} = \frac{\alpha_{RNFL}(e^{2\mu_{RNFL} d_{RNFL}} - 1)}{\alpha_{RPE}(1 - e^{-2\mu_{RPE} d_{RPE}})}, \quad (19)$$

where S is the total OCT signal in a given depth range, γ is the conversion factor, α is the fraction of light at the layer of interest, and I_0 is the incident light intensity. Equation 19 can be simplified by combining the constant terms and finding an optimal fit, which allows the authors to arrive at a constant: β ($\beta = 2.3$). The final expression is shown in Equation 20, where μ is the AC of the RNFL determined per A-scan, R is the intensity ratio of the RNFL and RPE, and d_{RNFL} is the thickness of the RNFL:

$$\mu = \frac{\log(\frac{R}{\beta} + 1)}{2 \cdot d_{RNFL}}. \quad (20)$$

In total we calculated 20 AC measurements from the 20-A-scan region for every B-scan. We then determined one AC value for each B-scan by averaging the 20 A-scan AC measurements. Lastly, we averaged the AC measurements from the three B-scans we collected from each eye and used the averaged AC measurement for statistical analysis.

AC calculations with the DRC method: We generated AC mappings for the corresponding B-scans with the DRC algorithm. The DRC is based on the original depth-resolved method, introduced by Vermeer et al. in 2014. Here, the light intensity is modeled as

$$I(z) = A\gamma h(z)\mu(z)I_0 e^{-2\int_0^z \mu(u)du}, \ (21)$$

where A is the backscattering ratio. The AC, accounting for a maximum imaging depth D, can be solved as

$$\mu(z) = \frac{I(z)}{2\int_z^\infty I(u)du} \approx \frac{I(z)}{2\int_z^D I(u)du}. \ (22)$$

The discretized AC measurement for each pixel i with pixel size Δ is given by

$$\mu[i] = \frac{1}{2\Delta}\log\left(1 + \frac{I[i]}{\Sigma_{i+1}^\infty I[i]}\right), \ (23)$$

and thus a cross-sectional AC mapping is generated per B-scan with pixel-wise AC estimation.

For a direct comparison with the LIR results, the same 20-pixel-wide region was selected from the AC mapping for estimation. Because the DRC method provided pixel-wise calculation of AC (that is, it produces an AC value for every pixel within an A-scan), we took the mean of the depth-dependent ACs in the RNFL region for each A-scan to yield 20 averaged A-scan AC measurements per B-scan. Then, we calculated one AC value for each B-scan by averaging the 20 A-scan AC measurements. Lastly, we determined an averaged AC measurement for each eye from its three B-scans.

3.2.6 Statistical Analysis

Statistical analysis of differences between pairs of study groups on the testing parameters (AC_{LIR}, AC_{DRC} and depth-dependent AC parameters) were based on the nonparametric Mann-Whitney U test. Comparisons between the LIR and DRC methods were done through the Wilcoxon matched pair test. To compare the patient information and scan quality across all study groups, we used Kruskal-Wallis test, where Gaussian distributions were not assumed. VA measurements were converted into the LogMAR scale for statistical analysis.

3.3 Results

3.3.1 Participant Demographics

We imaged and analyzed 44 eyes from healthy volunteers and from patients presenting to the Vanderbilt Eye Institute who were previously diagnosed with glaucoma or high risk of glaucoma. Of the 44 eyes, 10 were considered glaucoma suspects, 12 had mild-stage glaucoma, 12 had moderate- or severe-stage glaucoma, and 10 were healthy controls. Note that four healthy eyes analyzed in the study have had cataract surgery and had an intraocular lens implant present at the time of imaging. Table 1 shows the mean and standard deviation of patient age, IOP and VA of eyes included in each study group. The mean ages of the healthy group, glaucoma-suspect group, mild glaucoma group, and moderate/severe glaucoma group were 72.3, 71.5, 70.4, and 71.2, respectively. There were no significant differences among the mean ages of the study groups ($p = 0.85$) and thus we considered our study groups as age-similar. Therefore, although aging is known to contribute to changes in the RNFL,[8] we can assume that the changes in AC that we observed among different study groups were not related to age but, rather, to disease progression. The IOP did not differ significantly across the study groups. In contrast, VA showed correlation with disease severity, as patients may have worse VA at more advanced glaucoma stages. We also recorded the signal strength of the scans, and the lowest recorded signal strength was 6/10. We did observe signal strength variations across the study groups. However, we did not expect that the differences in the signal strength would affect our measurements, as previous studies have shown that the small changes observed in the RNFL thickness when the signal strengths drop from 10/10 to 6/10 are not considered clinically significant.[48]

	Study subject statistics				
	Healthy	Glaucoma suspect	Mild glaucoma	Moderate/severe glaucoma	p-value
Age (years)	72.3 ± 9.9	71.5 ± 10.5	70.4 ± 12.6	71.2 ± 12.3	0.85
IOP (mmHg)	14.4 ± 3.1	15.5 ± 3.1	18.5 ± 4.1	15.5 ± 5.4	0.09
VA (LogMAR)	0.0 ± 0.05	0.17 ± 0.12	0.17 ± 0.12	0.26 ± 0.11	< 0.001
Signal strength	8.5 ± 0.9	8.3 ± 1.3	7.6 ± 1.0	6.6 ± 0.7	< 0.05
Sample Size	10	10	12	12	-

Table 1. Study subject statistics: Mean and standard deviation of age, intraocular pressure (IOP), visual acuity (VA), signal strength and sample size of each study group. The p-values, calculated for each row, indicate whether there are statistically significant differences among the study groups ($p \leq 0.05$ suggests statistically significant differences).

3.3.2 DRC vs. LIR

We studied whether the DRC method had comparable performance and produced similar results to LIR. Representative OCT B-scans and the corresponding AC mappings from healthy, glaucoma suspect, mild glaucoma and moderate/severe glaucoma eyes are shown in the top two rows of Figure 8. When comparing across the disease stages, the AC mapping allows direct visualization of disease progression, with decreasing AC values in the more severely impacted RNFL. The bottom row of Figure 8 shows the depth-dependent AC measurements (solid pink line) and mean AC (dashed pink line) from the DRC method and the single-valued AC calculated from the LIR method (solid blue line) for the A-scan denoted with an arrow in the middle row.
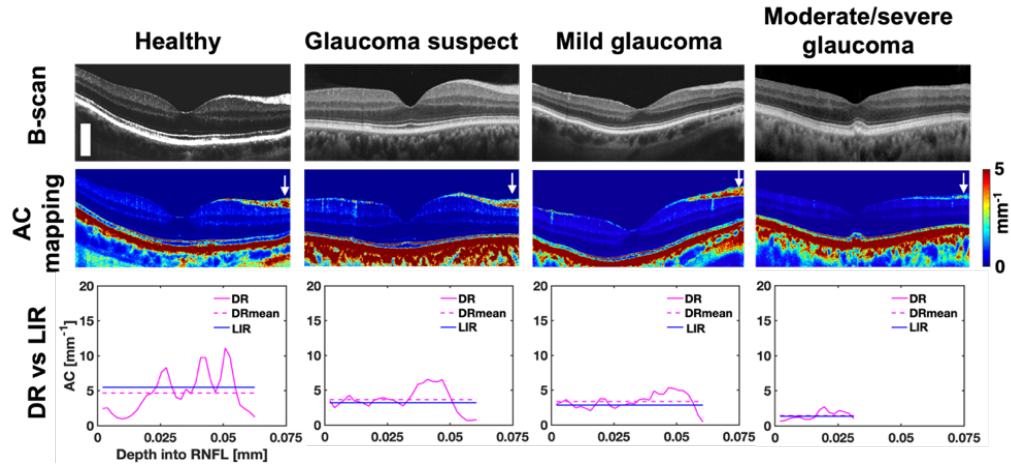
Figure 8. OCT B-scans and corresponding AC mappings of healthy (OS), glaucoma suspect (OS), mild glaucoma (OS) and moderate/severe glaucoma eyes (OS); bottom row shows extracted depth-dependent AC value by the DRC method and LIR method from the A-scan indicated by the white arrow. OS: left eye. Scale bar: 0.25 mm.

DRC and LIR yield comparable AC estimations without statistically significant differences ($p > 0.5$ for all severity groups). The average AC measurements, AC_{DRC} and AC_{LIR}, are plotted in Figure 9 for the DRC method and LIR method, respectively.
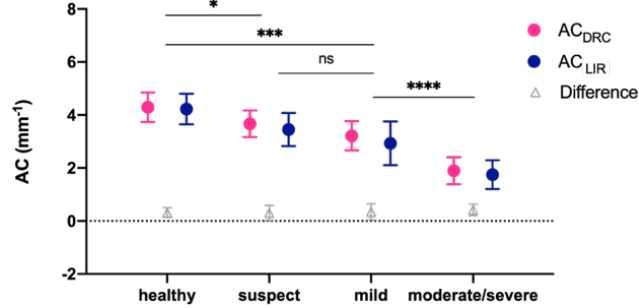
Figure 9. ACs from DRC and LIR and the calculated differences (absolute value shown in plot) between the two methods in healthy and glaucomatous eyes. * p < 0.05, *** p < 0.005, ns: no significance. p values shown on plot are calculated based on AC_{DRC}. Error bars represent standard deviations.

The estimated AC values from AC_{DRC} and AC_{LIR} are 4.15 (95% C.I. 3.72 - 4.58) vs. 3.91 (95% C.I. 3.39 - 4.43) mm^{-1}, 2.98 (95% C.I. 2.25 – 3.71) vs. 2.84 (95% C.I. 2.05 – 3.62) mm^{-1}, 3.13 (95% C.I. 2.74 – 3.52) vs. 2.84 (95% C.I. 2.28 – 3.40) mm^{-1} and 2.37 (95% C.I. 1.82 – 2.91) vs. 2.16 (95% C.I. 1.58 – 2.74) mm^{-1} for healthy, glaucoma suspect, mild glaucoma and moderate/severe stage glaucoma, respectively. Note that the ACs for both methods are able to distinguish healthy eyes from glaucoma suspects and glaucomatous eyes. Table 2 reports the estimated AC values from the two algorithms for each severity group and tests for statistical differences between the results from the two algorithms. Differences between the groups were not statistically significant (p value < 0.05 is considered significantly different).

	RNFL attenuation coefficient measurements							
	Healthy		Glaucoma suspect		Mild glaucoma		Moderate/severe glaucoma	
	mean	p-value	mean	p-value	mean	p-value	mean	p-value
AC_{DRC} [mm^{-1}]	4.15	0.11 (ns)	2.98	0.16 (ns)	3.13	0.34 (ns)	2.37	0.13 (ns)
AC_{LIR} [mm^{-1}]	3.91		2.84		2.84		2.16	

*ns: not significant.

Table 2. Mean RNFL attenuation coefficient calculated from layer intensity ratio (ACLIR) and depth-resolved (ACDRC) methods measured in healthy eyes and glaucomatous eyes [mm-1].

3.4 Discussion and Conclusion

In this study, we applied depth-resolved AC analysis with the DRC algorithm to the detection of early-stage glaucoma and showed that it has comparable performance to the LIR method when analyzed with averaged AC values. The results in Figure 9 and Table 3.2 do not show statistically significant differences when comparing the ACs extracted by DRC and LIR method from each study group, which suggests that DRC is as effective at predicting ACs from the RNFL as LIR and can be used to derived diagnostic metrics for evaluating pathological changes.

A previous study has shown that the AC can successfully differentiate glaucomatous eyes from healthy ones.(22) However, the disease population in that study was restricted to moderate glaucoma. In our study, we show that the mean AC is a valuable metric for detecting even early-stage glaucoma by including a mild glaucoma group as well as a glaucoma-suspect group. Comparing the mean AC across study groups, we observe a decrease in the measurement as the disease stage advances. This decrease can be explained by the reduced density of nerve fibers and retinal capillaries, both of which have been shown in the progression of glaucoma.(7, 22) This explanation is also supported by the finding of the decrease in the RNFL birefringence in glaucoma patients, as the alignment of axons is disrupted when axonal death occurs.(19, 49)

A major advantage of the DRC algorithm is that it does not require segmentation of the retinal layers (i.e., RNFL, RPE, or GCL) to obtain attenuation coefficient measurements. Moreover, it is robust against cases of a thin RNFL or irregularly shaped retina; whereas, segmentation of the RNFL is more likely to fail and would result in inaccurate calculation of the attenuation coefficients using the curve-fitting or the LIR algorithm. While automated segmentation could remove a barrier to LIR implementation, DRC still holds

an advantage that it enables visualization of pixel-wise changes of the RNFL in cross-section, which may enable detection of earlier glaucomatous changes that would otherwise be missed from a regular OCT image or an *en face* AC mapping. In cases where an averaged regional reading from the AC map, or quantitative, depth-dependent AC measurements were to be desired, AC-enabled auto-segmentation could be easily incorporated, and has been shown to yield superior performance for segmentation than its intensity-based alternatives.(50, 51)

CHAPTER 4

Definition of Novel AC-based Biomarkers for Detection of Early-Stage Glaucoma

4.1 Abstract

The ability of the DRC to extract depth-wise information also enables us to extract new metrics (the slope and the residual) to describe the changes of AC along depth. We find that the information extracted from the depth-dependent AC may add diagnostic value. Therefore, in this chapter, further investigations are performed on the depth-resolved AC measurement, and we compare the extracted values from the four study groups. Additionally, biological reasonings behind the observed changes are discussed.

4.2 Materials and Methods

4.2.1   Human Subject Recruitment

This study was performed under approval from the Institutional Review Board of Vanderbilt University (IRB #190937). We recruited patients presenting to the Vanderbilt Eye Institute who were previously diagnosed with glaucoma or high risk of glaucoma based on standard-of-care methods, including a visual field test, biomicroscopy and OCT. Informed consent was obtained after thorough explanation of the study. Glaucoma severity was determined by the mean deviation (MD) of the visual field test (Humphrey field analyzer II, Carl Zeiss Meditec), where mild glaucoma cases had an MD ranging from 0 to -6.0 dB and moderate/severe cases had an MD worse than -6.0 dB. Eyes with visual acuity (VA) worse than 20/50 were excluded from analysis. Glaucoma suspects were identified by clinicians: these patients had high risk of glaucoma by showing some suspicious feature during exam, such as optic nerve asymmetry, a family history of glaucoma, or a high intraocular pressure (IOP), but had not shown functional damage on the visual field test or thinning of the RNFL on OCT scans. Age-similar healthy volunteers were recruited as a control population. For inclusion, healthy participants needed to have a healthy eye history (except for uncomplicated cataract surgery), IOP of 21 mm Hg or lower, no signs of glaucoma when examining the optic nerve appearance and 20/25 or better VA. Individuals with a visually significant cataract (without receiving surgery) were excluded from the study, to avoid poor signal quality.

4.2.2   Definition of Depth-Dependent AC parameters

A main advantage of the DRC method is that the AC can be calculated per pixel, which provides depth-dependent information. By plotting pixel-wise AC measurements, we can visually observe changes in the AC at different depths in the RNFL, as shown in the bottom row of Figure 8. For most regions, we noticed a roughly linear, increasing trend in the AC vs. depth relationship, with some amplitude fluctuation (larger fluctuations in healthier RNFLs and smaller fluctuations in the RNFLs of more advanced glaucoma severity). To quantify the rate of increase and the amount of fluctuation of the AC measurements along depth, we applied linear regression to define two parameters to describe the local changes of the AC: the slope and the fitting residual.

For a given A-scan, we first normalized the depth vector, whose range comprises the thickness of the RNFL. Next, we performed linear regression on the depth-resolved AC as a function of normalized depth for each A-scan, where we determined a fitting slope and an averaged absolute fitting residual from each. An example plot of the depth-resolved AC from a single A-scan and the linear fit is shown in Figure 10 (a). To reduce the fitting error and find the most linear region, five pixels near the top and bottom surface of the RNFL were excluded from the analysis, as AC values tend to decrease dramatically near the layer interface. As a result, two eyes from the moderate/severe group did not have sufficient data points in the RNFL for performing the linear regression and therefore were excluded from analysis. Then, we repeated the same calculation for all 20 A-scans in the region of interest and computed a mean fitting slope and absolute fitting residual for each B-scan. Lastly, we determined the values of depth-dependent parameters for a given eye by averaging the measurements from its three B-scans and used the averaged values in the statistical analysis.
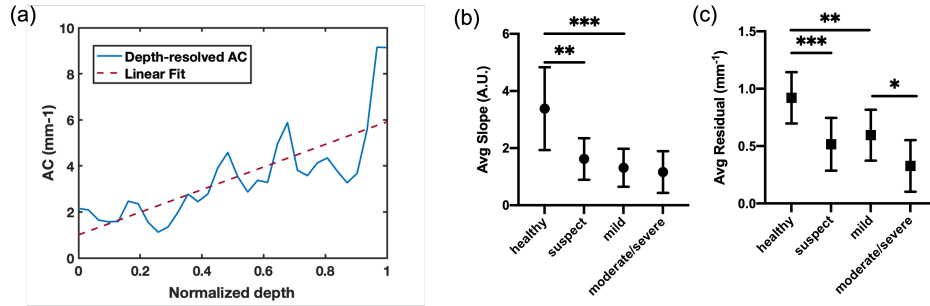
Figure 10. Depth-dependent AC analysis of the RNFL. (a) Depth-resolved AC plotted against normalized depth. (a) Depth-resolved AC plotted against normalized depth. (b) Averaged fitting slope of each study group. (c) Averaged absolute fitting residual of each study group. * p < 0.05, ** p < 0.01, *** p < 0.005.

4.3 Results

4.3.1   Participant Demographics

We imaged and analyzed 44 eyes from healthy volunteers and from patients presenting to the Vanderbilt Eye Institute who were previously diagnosed with glaucoma or high risk of glaucoma. Of the 44 eyes, 10 were considered glaucoma suspects, 12 had mild-stage glaucoma, 12 had moderate- or severe-stage glaucoma, and 10 were healthy controls. The mean ages of the healthy group, glaucoma suspect group, mild glaucoma group, and moderate/severe glaucoma group were 72.3, 71.5, 70.4, and 71.2, respectively.

4.3.2   Statistical Analysis on B-Scan Datasets

Our results indicate that there is more rapid increase and larger fluctuations in the pixel-wise ACs as a function of depth in the healthy RNFL than the diseased RNFL. The mean fitting slope and fitting residual for each study group are shown in Figure 10 (b) and (c). The fitting slope measurement can differentiate suspect eyes and mild glaucoma eyes from the healthy eyes ($p < 0.01$ and $p < 0.005$, respectively) with higher statistical significances than the mean AC measurements ($p < 0.05$). The statistical significance improves when differentiating the suspect eyes from the healthy with the fitting residual ($p < 0.005$).

4.4 Discussion and Conclusion

We reason that the depth-dependent increase in AC near the outer surface of the RNFL is due to the presence of radial peripapillary capillaries (RPC), which are long, straight vessels that run parallel with the RNFL axons and are located near the RNFL and ganglion cell layer interface.(52, 53) In the study of Cambell et al., the authors reported an increasing capillary density as a function of depth in the RNFL (Figure 11), which agrees with the trend we observed in the depth-resolved AC data.(52)
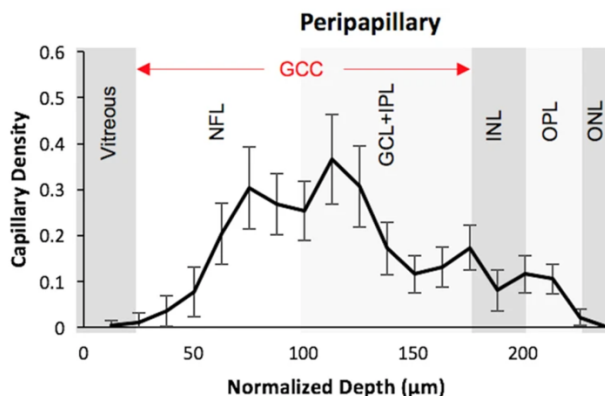
Figure 11. Retinal capillary density as a function of normalized depth and structural optical coherence tomography layers. (Adapted from: Campell et al., Sci Rep. (2017)).

Therefore, we reason that the AC in the RNFL is associated with a combination of scattering and absorption of light, where the RNFL axons contribute to the scattering and the blood in the RPC contributes to the absorption. The decrease in the slope of the depth-resolved AC in glaucoma takes into the account the reduction in the densities of both the nerve axon as well as the capillaries. The decrease in the fluctuations of the AC along depth in more severe glaucoma cases may be explained by the loss of RPC density due to glaucoma progression, as the capillary density has been reported as significantly lower in glaucomatous eyes than healthy eyes, shown in Figure 12.(7, 54, 55)
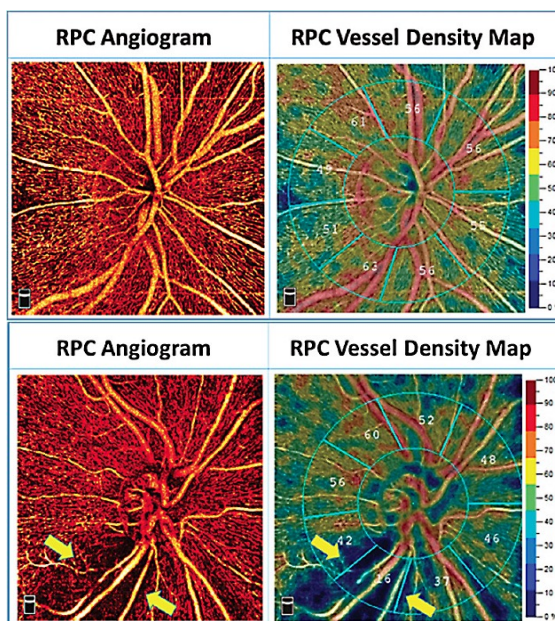
Figure 12. Radial peripapillary capillary angiograms and vessel density maps of healthy (top) and glaucomatous (bottom) eye. (Adapted from: Mansoori et al., Saudi Journal of Ophthalmology. (2018)).

When compared to the RNFL reflectance, the depth-dependent AC analysis may be a more reliable measurement because it measures the rate of signal decay and is independent of the signal strength.(21) Both the reflectivity and the birefringence of the RNFL have been shown to be more sensitive to disease progression than thickness measurements in glaucoma, and it was reasoned in the literature that the disruption of the integrity of the axonal cytoskeleton caused by glaucoma could lead to changes in the reflectivity and birefringence in early onset glaucoma and even glaucoma-suspect patients, which precedes noticeable reduction in the RNFL thickness.(10, 19) Since the AC is the measurement of the rate of light attenuation and is inherently correlated with reflectivity and tissue birefringence, we expect that the AC, too, could serve as a diagnostic parameter to enable earlier detection and more accurate monitoring of glaucoma.

CHAPTER 5

Conclusions

5.1 Summary and Conclusion

Detecting early-stage glaucoma remains a challenge in current clinical practice. In this study we assessed the ability of the optical attenuation coefficient (AC) of the retinal nerve fiber layer (RNFL) to detect early-stage glaucoma, compared the performance of two AC extraction algorithms, and introduced new depth-dependent diagnostic parameters. Our results suggest that the AC is a promising parameter for early glaucoma detection in addition to measurements obtained from conventional retinal OCT scans, such as RNFL thickness. We also showed that depth-dependent AC analysis is an even more sensitive measure to monitor and detect early signs of glaucoma.

5.2 Recommendation for Future Directions

It is important to note that both the original depth-resolved algorithm and DRC make the assumption that the light intensity decays to zero at the end of the imaging range.(32, 42) However, when this assumption is not true, the resulting AC values suffer from over-estimation for pixels near the bottom of the image.(45, 56) In this paper, the retinal structure of interest, the RNFL, was placed in the top half of each B-scan; therefore, our analysis only minimally suffers by not implementing an end-of-range correction. Note that this issue would be problematic if one were to study tissue structures located near the end of the imaging range, as the AC values could peak and lead to erroneous mean AC, as well as an erroneous depth-dependent AC analysis. Solutions have been proposed to address this issue, where over-estimation is corrected for in pixels near the bottom of the image.(45) This correction should be incorporated into the depth-resolved AC extraction algorithm in future studies for more accurate estimations.

A limitation of this study is that, due to the availability of data, we only acquired high-resolution images and corresponding analysis of a limited area of the RNFL: the temporal region. This limitation may explain the overlap of AC values between the healthy and early-stage glaucoma eyes, as glaucoma may have affected the superior or the inferior quadrants more dramatically than the area where we took the measurement. However, the promising results shown in the depth-dependent AC analysis encourage future studies in all quadrants of the optic nerve with a greater number of patients. Another limitation was the use of manual segmentation to perform the analysis. This was done because reliable automatic segmentation of the RPE for the high-resolution line scan data was not available at the time of the experiment. However, such algorithms are widely available for volumetric data for the ONH. As one proceeds to the collection of volumetric data for further research, they should adopt automatic segmentation approaches for more efficient analysis.

5.3 Contribution to the Field and Societal Impact

Many new diagnostics biomarkers with potential to detect earlier changes in the RNFL than the thickness measurement have been proposed in recent literature, including RNFL birefringence(19, 49, 57) and reflectance,(10, 58) which are tissue-optical-property-based metrics. Although studies have shown promising results for the RNFL birefringence in differentiation of early-stage glaucoma,(49, 57) this method relies on the use of polarization-sensitive OCT, which greatly hinders its potential for clinical translation because the generation and analysis of polarized light requires additional components, which adds to the overall expense and complexity of the system. The AC, which is also based on tissue optical properties, may be a complementary or even superior metric to the clinical standards, such as the RNFL thickness measurement. A previous study has demonstrated the structure-function correlation of AC to the mean deviation of the visual field test in glaucoma population.(23) When compared to thickness-based analysis, such as in the RNFL or GCL, the AC measurement may be less affected by natural biological variation,(17, 59) as the ACs are based on the contrast of internal tissue structures. When compared to other emerging tissue-optical-property metrics, the DRC method and the depth-dependent AC parameter

extraction we use here can be performed on currently available OCT systems that are already widely distributed in clinical practices worldwide.

Additionally, our study reports the AC from glaucoma-suspect patients, which is a population that was omitted by previous studies on the AC. The AC measured from this group falls between the ACs of the normal and the confirmed glaucoma population. Longitudinal studies on glaucoma-suspect patients may reveal the potential of AC and depth-resolved AC analysis for establishing a threshold for the possibility of the actual development of glaucoma in these patients. The healthcare benefits of deploying this analysis are that it could serve as a form of triage that could permit more efficient dedication of clinical resources to follow-up and provide timely treatment to true glaucoma patients, as the current clinic is overpopulated by glaucoma suspects.

In summary, the use of the AC as extracted from the DRC has strong potential to assist with clinical evaluation of early-stage glaucoma. To this end, a strong advantage of the method we proposed in the paper is that it introduces minimal changes to the current clinical workflow, as it does not require extra hardware or extensive data collection. The limitations of the current study include the small sample size, as well as the limited region of analysis. A volumetric analysis of the depth-dependent AC in the entire region of the ONH is recommended for future studies, where retinal volume scans should be acquired from a larger number of participants, the AC_{RNFL} could be extracted from all quadrants for analysis and a classifier could be built for assessing the performance of these newly defined metrics against the traditional ones, such as thickness measurements.

References

1. Adelson JD, Bourne RRA, Briant PS, Flaxman SR, Taylor HRB, et al. 2020. Causes of blindness and vision impairment in 2020 and trends over 30 years, and prevalence of avoidable blindness in relation to VISION 2020: the Right to Sight: an analysis for the Global Burden of Disease Study. *Lancet Glob. Heal.*

2. Leung CK, Cheung CY, Weinreb RN, Qiu Q, Liu S, et al. 2009. Retinal Nerve Fiber Layer Imaging with Spectral-Domain Optical Coherence Tomography: A Variability and Diagnostic Performance Study. *Ophthalmology*. 116(7):1257-1263.e2

3. Kanamori A, Nakamura M, Escano MFT, Seya R, Maeda H, Negi A. 2003. Evaluation of the glaucomatous damage on retinal nerve fiber layer thickness measured by optical coherence tomography. *Am. J. Ophthalmol.* 135(4):513–20

4. Medeiros FA, Zangwill LM, Bowd C, Vessani RM, Susanna R, Weinreb RN. 2005. Evaluation of retinal nerve fiber layer, optic nerve head, and macular thickness measurements for glaucoma detection using optical coherence tomography. *Am. J. Ophthalmol.* 139(1):44–55

5. Savini G, Zanini M, Carelli V, Sadun AA, Ross-Cisneros FN, Barboni P. 2005. Correlation between retinal nerve fibre layer thickness and optic nerve head size: An optical coherence tomography study. *Br. J. Ophthalmol.* 89(4):489–92

6. Budenz DL, Anderson DR, Varma R, Schuman J, Cantor L, et al. 2007. Determinants of Normal Retinal Nerve Fiber Layer Thickness Measured by Stratus OCT. *Ophthalmology*. 114(6):1046–52

7. Mansoori T, Gamalapati J, Sivaswamy J, Balakrishna N. 2018. Optical coherence tomography angiography measured capillary density in the normal and glaucoma eyes. *Saudi J. Ophthalmol.* 32(4):295–302

8. Parikh RS, Parikh SR, Sekhar GC, Prabakaran S, Babu JG, Thomas R. 2007. Normal Age-Related Decay of Retinal Nerve Fiber Layer Thickness. *Ophthalmology*. 114(5):921–26

9. Leung CKS, Lam AKN, Weinreb RN, Garway-Heath DF, Yu M, et al. 2022. Diagnostic assessment of glaucoma and non-glaucomatous optic neuropathies via optical texture analysis of the retinal nerve fibre layer. *Nat. Biomed. Eng.*

10. Huang X-R, Zhou Y, Kong W, Knighton RW. 2011. Reflectance decreases before thickness changes in the retinal nerve fiber layer in glaucomatous retinas. *Invest. Ophthalmol. Vis. Sci.* 52(9):6737–42

11. Zotter S, Pircher M, Götzinger E, Torzicky T, Yoshida H, et al. 2013. Measuring retinal nerve fiber layer birefringence, retardation, and thickness using wide-field, high-speed polarization sensitive spectral domain OCT. *Investig. Ophthalmol. Vis. Sci.* 54(1):72–84

12. Dong ZM, Wollstein G, Schuman JS. 2016. Clinical utility of optical coherence tomography in glaucoma. *Investig. Ophthalmol. Vis. Sci.* 57(9Special Issue):OCT556–67

13. Huang D, Swanson EA, Lin CP, Schuman JS, Stinson WG, et al. 1991. Optical coherence tomography. *Science*. 254(5035):1178–81

14. Park Hae Young L, Park Chan K. 2013. Structure-Function Relationship and Diagnostic Value of RNFL Area Index Compared With Circumpapillary RNFL Thickness by Spectral-Domain OCT. *J. Glaucoma*. 22(2):88–97

15. Pons ME, Ishikawa H, Gürses-Özden R, Liebmann JM, Dou HL, Ritch R. 2000. Assessment of retinal nerve fiber layer internal reflectivity in eyes with and without glaucoma using optical coherence tomography. *Arch. Ophthalmol.*

16. Kim MJ, Lee EJ, Kim TW. 2010. Peripapillary retinal nerve fibre layer thickness profile in subjects with myopia measured using the Stratus optical coherence tomography. *Br. J. Ophthalmol.* 94(1):115–20

17. Kang SH, Hong SW, Im SK, Lee SH, Ahn MD. 2010. Effect of myopia on the thickness of the retinal nerve fiber layer measured by cirrus HD optical coherence tomography. *Investig. Ophthalmol. Vis. Sci.* 51(8):4075–83

18. Seo S, Lee CE, Jeong JH, Park KH, Kim DM, Jeoung JW. 2017. Ganglion cell-inner plexiform layer and retinal nerve fiber layer thickness according to myopia and optic disc area: A quantitative and three-dimensional analysis. *BMC Ophthalmol.* 17(1):1–8

19. Huang X-R, Knighton RW, Spector YZ, Qiao J, Kong W, Zhao Q. 2017. Reflectance Spectrum and Birefringence of the Retinal Nerve Fiber Layer With Hypertensive Damage of Axonal Cytoskeleton. *Invest. Ophthalmol. Vis. Sci.* 58(4):2118–29

20. Xu J, Ishikawa H, Wollstein G, Bilonick RA, Folio LS, et al. 2013. Three-Dimensional Spectral-Domain Optical Coherence Tomography Data Analysis for Glaucoma Detection. *PLoS One*. 8(2):e55476

21. Gardiner SK, Demirel S, Reynaud J, Fortune B. 2016. Changes in retinal nerve fiber layer reflectance intensity as a predictor of functional progression in Glaucoma. *Investig. Ophthalmol. Vis. Sci.* 57(3):1221–

22. Vermeer KA, van der Schoot J, Lemij HG, de Boer JF. 2012. RPE-normalized RNFL attenuation coefficient maps derived from volumetric OCT imaging for glaucoma assessment. *Investig. Ophthalmol. Vis. Sci.* 53(10):6102–8

23. van der Schoot J, Vermeer KA, de Boer JF, Lemij HG. 2012. The effect of glaucoma on the optical attenuation coefficient of the retinal nerve fiber layer in Spectral Domain Optical Coherence Tomography images. *Investig. Ophthalmol. Vis. Sci.* 53(4):2424–30

24. Muller BG, van Kollenburg RAA, Swaan A, Zwartkruis ECH, Brandt MJ, et al. 2018. Needle-based optical coherence tomography for the detection of prostate cancer: a visual and quantitative analysis in 20 patients. *J. Biomed. Opt.* 23(08):1

25. Freund JE, Faber DJ, Bus MT, van Leeuwen TG, de Bruin DM. 2019. Grading upper tract urothelial carcinoma with the attenuation coefficient of in-vivo optical coherence tomography. *Lasers Surg. Med.* lsm.23079

26. Liu S. 2017. Tissue characterization with depth-resolved attenuation coefficient and backscatter term in intravascular optical coherence tomography images. *J. Biomed. Opt.* 22(09):1

27. Xu C, Schmitt JM, Carlier SG, Virmani R. 2008. Characterization of atherosclerosis plaques by measuring both backscattering and attenuation coefficients in optical coherence tomography. *J. Biomed. Opt.* 13(3):034003

28. Zhao Q, Zhou C, Wei H, He Y, Chai X, Ren Q. 2012. Ex vivo determination of glucose permeability and optical attenuation coefficient in normal and adenomatous human colon tissues using spectral domain optical coherence tomography. *J. Biomed. Opt.* 17(10):1050041

29. Baran U, Li Y, Wang RK, Aran UTKUB, Uandong YLI. 2015. In vivo tissue injury mapping using optical coherence tomography based methods. *Appl. Opt.* 54(21):6448–53

30. Rodriguez CLR, Szu JI, Eberle MM, Wang Y, Hsu MS, et al. 2014. Decreased light attenuation in cerebral cortex during cerebral edema detected using optical coherence tomography. *Neurophotonics*. 1(2):025004

31. Dwork N, Smith GT, Leng T, Pauly JM, Bowden AK. 2019. Automatically determining the confocal parameters from OCT B-Scans for quantification of the attenuation coefficients. *IEEE Trans. Med. Imaging*. 38(1):261–68

32. Vermeer KA, Mo J, Weda JJA, Lemij HG, de Boer JF. 2014. Depth-resolved model-based reconstruction of attenuation coefficients in optical coherence tomography. *Biomed. Opt. Express*. 5(1):322

33. Faber DJ, van der Meer FJ, Aalders MCG, van Leeuwen TG. 2004. Quantitative measurement of attenuation coefficients of weakly scattering media using optical coherence tomography. *Opt. Express*. 12(19):4353

34. Almasian M, Bosschaart N, van Leeuwen TG, Faber DJ. 2015. Validation of quantitative attenuation and backscattering coefficient measurements by optical coherence tomography in the concentration-dependent and multiple scattering regime. *J. Biomed. Opt.*

35. Scolaro L, Robbins PD, Sampson DD, Saunders CM, Wood BA, et al. 2012. Parametric imaging of the local attenuation coefficient in human axillary lymph nodes assessed using optical coherence tomography. *Biomed. Opt. Express*. 3(2):366

36. van der Schoot J, Vermeer KA, de Boer JF, Lemij HG. 2012. The effect of glaucoma on the optical attenuation coefficient of the retinal nerve fiber layer in Spectral Domain Optical Coherence Tomography images. *Investig. Ophthalmol. Vis. Sci.* 53(4):2424–30

37. Thrane L, Yura HT, Andersen PE. 2000. Analysis of optical coherence tomography systems based on the extended Huygens-Fresnel principle. *J. Opt. Soc. Am. A*. 17(3):484–90

38. Knu A, Bonev S, Knaak W. 2018. New method for evaluation of in vivo scattering and refractive index properties obtained with optical coherence tomography. . 9(2):265–73

39. Levitz D, Thrane L, Frosz MH, Andersen PE, Andersen CB, et al. 2004. Determination of optical scattering properties of highly-scattering media in optical coherence tomography images. *Opt Express*. 12(2):249–59

40. Vermeer KA, van der Schoot J, Lemij HG, de Boer JF. 2012. Quantitative RNFL attenuation coefficient measurements by RPE-normalized OCT data. *Ophthalmic Technol. XXII*. 8209(March 2012):82090U

41. S. H. Yun, G. J. Tearney, B. E. Bouma, B. H. Park and JF de B. 2003. High-speed spectral-domain optical coherence tomography at 1.3 um wavelength. *Opt. Express*. 11(26):3598–3604

42. Smith GT, Dwork N, O'Conner D, Sikora U, Lurie KL, et al. 2015. Automated, Depth Resolved Estimation of Attenuation Coefficient From Optical Coherence Tomography Data. *IEEE Trans. Med. Imaging*. 34(12):2592–2602

43. Quigley HA, Addicks EM, Green WR. 1982. Optic Nerve Damage in Human Glaucoma: III. Quantitative Correlation of Nerve Fiber Loss and Visual Field Defect in Glaucoma, Ischemic Neuropathy, Papilledema,

and Toxic Neuropathy. *JAMA Ophthalmol.* 100(1):135–46

44.   Huang X-R, Knighton RW, Cavuoto LN. 2006. Microtubule Contribution to the Reflectance of the Retinal Nerve Fiber Layer. *Invest. Ophthalmol. Vis. Sci.* 47(12):5363–67

45.   Liu J, Ding N, Yu Y, Yuan X, Luo S, et al. 2019. Optimized depth-resolved estimation to measure optical attenuation coefficients from optical coherence tomography and its application in cerebral damage determination. *J. Biomed. Opt.* 24(3):1–11

46.   Rothman AL, Sevilla MB, Freedman SF, Tong AY, Tai V, et al. 2015. Assessment of retinal nerve fiber layer thickness in healthy, full-term neonates. *Am. J. Ophthalmol.* 159(4):803–11

47.   van der Schoot J, Vermeer KA, de Boer JF, Lemij HG. 2012. The effect of glaucoma on the optical attenuation coefficient of the retinal nerve fiber layer in Spectral Domain Optical Coherence Tomography images. *Investig. Ophthalmol. Vis. Sci.* 53(4):2424–30

48.   Samarawickrama C, Pai A, Huynh SC, Burlutsky G, Wong TY, Mitchell P. 2010. Influence of OCT signal strength on macular, optic nerve head, and retinal nerve fiber layer parameters. *Investig. Ophthalmol. Vis. Sci.* 51(9):4471–75

49.   Desissaire S, Pollreisz A, Sedova A, Hajdu D, Datlinger F, et al. 2020. Analysis of retinal nerve fiber layer birefringence in patients with glaucoma and diabetic retinopathy by polarization sensitive OCT. *Biomed. Opt. Express*. 11(10):5488

50.   Novosel J, Wang Z, De Jong H, Van Velthoven M, Vermeer KA, Van Vliet LJ. 2016. Locally-adaptive loosely-coupled level sets for retinal layer and fluid segmentation in subjects with central serous retinopathy. *Proc. - Int. Symp. Biomed. Imaging*. 2016-June(April):702–5

51.   Callewaert T, Dik J, Kalkman J. 2017. Segmentation of thin corrugated layers in high-resolution OCT images. *Opt. Express*. 25(26):32816

52.   Campbell JP, Zhang M, Hwang TS, Bailey ST, Wilson DJ, et al. 2017. Detailed Vascular Anatomy of the Human Retina by Projection-Resolved Optical Coherence Tomography Angiography. *Sci. Rep.* 7(January):1–11

53.   Mase T, Ishibazawa A, Nagaoka T, Yokota H, Yoshida A. 2016. Radial peripapillary capillary network visualized using wide-field montage optical coherence tomography angiography. *Investig. Ophthalmol. Vis. Sci.* 57(9):504–10

54.   Chen CL, Zhang A, Bojikian KD, Wen JC, Zhang Q, et al. 2016. Peripapillary retinal nerve fiber layer vascular microcirculation in glaucoma using optical coherence tomography–based microangiography. *Investig. Ophthalmol. Vis. Sci.* 57(9):475–85

55.   Yarmohammadi A, Zangwill LM, Diniz-Filho A, Suh MH, Manalastas PI, et al. 2016. Optical coherence tomography angiography vessel density in healthy, glaucoma suspect, and glaucoma eyes. *Investig. Ophthalmol. Vis. Sci.* 57(9):OCT451–59

56.   Chang S, Bowden AK. 2019. Review of methods and applications of attenuation coefficient measurements with optical coherence tomography. *J. Biomed. Opt.* 24(9):

57.   Gotzinger E, Pircher M, Baumann B, Resch H, Vass C, Hitzenberger CK. 2009. Comparison of Retinal Nerve Fiber Layer Birefringence and Thickness of Healthy and Glaucoma Suspect Eyes Measured with Polarization Sensitive Spectral Domain OCT. *Invest. Ophthalmol. Vis. Sci.* 50(13):5823

58.   Huang X-R, Knighton RW, Feuer WJ, Qiao J. 2016. Retinal nerve fiber layer reflectometry must consider directional reflectance. *Biomed. Opt. Express*. 7(1):22

59.   Chung JK, Yoo YC. 2011. Correct calculation circle location of optical coherence tomography in measuring retinal nerve fiber layer thickness in eyes with myopic tilted discs. *Investig. Ophthalmol. Vis. Sci.* 52(11):7894–7900